Biodegradation and mechanical behavior of an advanced bioceramic-containing Mg matrix composite synthesized through in-situ solid-state oxidation

Naddaf Dezfuli, Sina; Brouwer, J. C.; Mol, J. M.C.; van der Helm, F. C.T.; Zhou, J.

DOI
10.1016/j.jmbbm.2018.01.014

Publication date
2018

Document Version
Final published version

Published in
Journal of the Mechanical Behavior of Biomedical Materials

Journal of the Mechanical Behavior of Biomedical Materials 80 (2018) 209–221

Contents lists available at ScienceDirect

Journal of the Mechanical Behavior of Biomedical Materials

journal homepage: www.elsevier.com/locate/jmbbm

Biodegradation and mechanical behavior of an advanced bioceramic-containing Mg matrix composite synthesized through in-situ solid-state oxidation

S. NaddafDezfuli[a,*], J.C. Brouwer[b], J.M.C. Mol[b], F.C.T. van der Helm[a], J. Zhou[a]

[a] Department of Biomechanical Engineering, Delft University of Technology, 2628 CD Delft, The Netherlands
[b] Department of Materials Science and Engineering, Delft University of Technology, 2628 CD Delft, The Netherlands

ARTICLE INFO

Keywords:
Magnesium
Composite
Chemical interlocking
Mechanical property
Degradation
Biocompatibility

ABSTRACT

Recent studies have shown great potential of Mg matrix composites for biodegradable orthopedic devices. However, the poor structural integrity of these composites, which results in excessive localized corrosion and premature mechanical failure, has hindered their widespread applications. In this research, an in-situ Powder Metallurgy (PM) method was used to fabricate a novel biodegradable Mg-bredigite composite and to achieve enhanced chemical interfacial locking between the constituents by triggering a solid-state thermochemical reaction between Mg and bredigite particles. The reaction resulted in a highly densified and integrated microstructure, which prevented corrosion pits from propagating when the composite was immersed in a physiological solution. In addition, chemical interlocking between the constituents prohibited interparticle fracture and subsequent surface delamination during compression testing, enabling the composite to withstand larger plastic deformation before mechanical failure. Furthermore, the composite was proven to be biocompatible and capable of maintaining its ultimate compressive strength in the strength range of cortical bone after 25-day immersion in DMEM. The research provided the necessary information to guide further research towards the development of a next generation of biodegradable Mg matrix composites with enhanced chemical interlocking.

1. Introduction

Magnesium, being among the lightest structural materials, is considered one of the biggest investment opportunities of this century (Luo, 2013). Magnesium is 75% lighter than steel, 50% lighter than titanium, and 33% lighter than aluminum (Kulekci, 2008; NaddafDezfuli et al., 2012). In the biomedical field, particularly in orthopedics, Mg stands out of the rest of the metals in the periodic table due to its biodegradable nature, high strength-to-density ratio and mechanical properties comparable to those of human bone (Witte, 2010).

However, Mg actively dissolves in physiological solutions at an undesirably high rate (NaddafDezfuli et al., 2014), leading to premature structure disintegration and subsequent loss of mechanical properties before the damaged bone is fully recovered. Lowering the degradation rate of Mg has been one of the most studied subjects in pursuit of clinically applicable Mg-based materials (Staiger et al., 2006).

Most of the previous attempts to slow down the biodegradation of Mg were focused on adding alloying elements such as aluminum and zirconium to Mg (Alvarez-Lopez et al., 2010; Hong et al., 2013; Liu et al., 2007), and quite a few, on developing Mg-matrix composites with bioactive particles embedded throughout the Mg matrix (Gu et al., 2010; Witte et al., 2007a; Zheng et al., 2010). Mg matrix composites use monolithic Mg as the metallic matrix so as to avoid possible toxic complications caused by alloying elements (Song, 2007). In addition, the chemical and mechanical properties of Mg matrix composites are adjustable by controlling material parameters such as bioceramic type, particle shape, sizes and distribution as well as processing conditions (NaddafDezfuli et al., 2017b).

In the previous research, Powder Metallurgy (PM) Mg matrix composites containing up to 40 vol% of bredigite were developed and these composites had integrated and homogenous microstructures and mechanical properties similar to those of human bone (NaddafDezfuli et al., 2017a, 2017b). However, the Mg matrix composites still suffered from premature inter-particle fracture and surface delamination under compressive loading (NaddafDezfuli et al., 2017b), causing the outer layer of specimen to be disintegrated from its core, which would be fatal in clinical cases. Inter-particle fracture and surface delamination were identified to be the two dominating failure mechanisms of the Mg matrix composites under mechanical loading, indicating that

* Corresponding author.
E-mail address: S.NaddafDezfuli@tudelft.nl (S. NaddafDezfuli).

https://doi.org/10.1016/j.jmbbm.2018.01.014
Received 22 November 2017; Received in revised form 11 January 2018; Accepted 15 January 2018

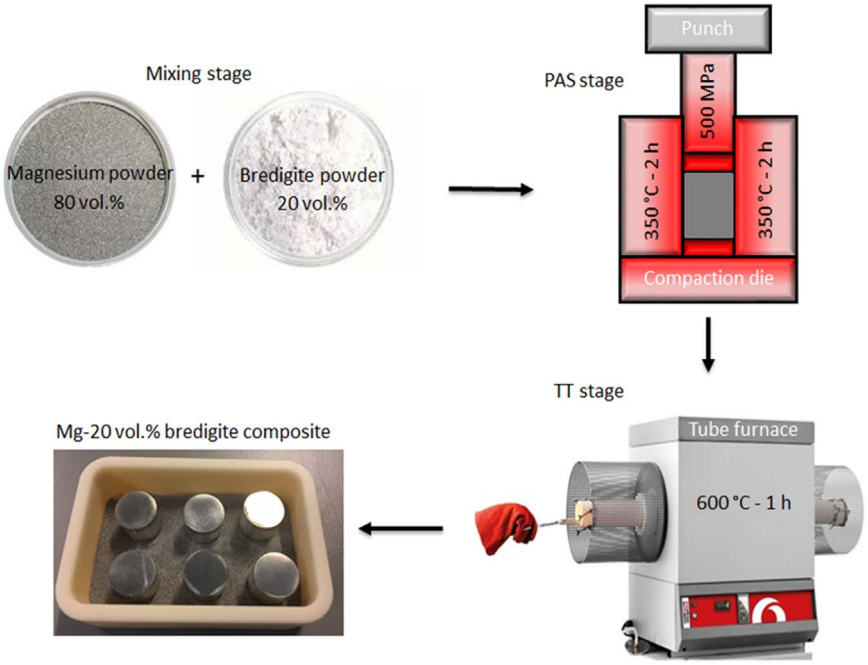

Fig. 1. Schematic illustration of the processing steps for the Mg–bredigite composite.

mechanical interlocking between Mg and bioceramic powder particles was not sufficiently strong to resist inter-particle fracture (NaddafDezfuli et al., 2017b). Inter-particle fracture became even more intense after the composites had been immersed in a physiological solution and suffered from localized corrosion at the edges of specimens. These localized corrosion sites in the Mg-matrix composites would provide nucleation sites for mechanical cracking, thereby reducing their durability if they were used for implants (Witte et al., 2005).

With the recognition of the weak spots in the composites developed earlier, there was a strong desire to improve the composites in terms of structural integrity, degradation behavior and mechanical properties. Improving the integrity of the Mg-bioceramic interface is a challenge because metals generally do not bond strongly with ceramics due to the differences in the nature of atomic bonding in metals and in ceramics (Askeland and Phulé, 2003). Nevertheless, there is a possibility to strengthen the metal-ceramic interface in Mg matrix composites, if an interlayer is formed, which allows chemical interlocking between the constituents. One way to achieve this is to trigger a thermochemical reaction at the Mg-bioceramic interface, causing atoms from both sides to swap by diffusion and forming an intermediate layer as a product of the reaction. The first criterion to achieve this would be the ability of magnesium to reduce oxide phases in bioceramic (e.g., SiO_2) into their elemental constituents (e.g., Si) through a solid state reaction. The second criterion would be the diffusivity of bioceramic elemental constituents into Mg crystal to establish a chemically integrated interface.

With these two criteria in mind, in this research, micro-sized bredigite powder particles was used (bredigite being a biodegradable ceramic in the CaO-MgO-SiO_2 family and known as a bioactive material with mechanical properties close to those of cortical bone and a stimulatory effect on osteoclast proliferation (Wu and Chang, 2007; Yi et al., 2014)), considering the fact that Mg is able to react with bredigite through a solid state oxidation reaction (NaddafDezfuli et al., 2017b), and the possible elemental products of the reaction (such as Si and Ca) are able to diffuse into Mg crystal (Kondoh et al., 2003; Zheng et al., 2010).

The goal of this study was to fabricate biodegradable Mg-bredigite composites with chemical bonding between powder particles, as an additional bonding mechanism to mechanical interlocking to prolong their service life by avoiding premature inter-particle fracture and delamination. Microstructure, mechanical and degradation behavior, in-vitro cytotoxicity and bioactivity of the newly developed composite were evaluated.

2. Materials and methods

2.1. In-situ synthesis of Mg matrix composite

A magnesium powder (containing 320 ppm Fe and 160 ppm Ni impurities – Shanghai Institute of Ceramics) with spherical particles and a mean particle size of 90 μm was mixed with a bredigite ($Ca_7MgSi_4O_{16}$ - Shanghai Institute of Ceramics) powder with a mean particle size of 10 μm and an irregular morphology by 20 vol%. Mixing lasted 12 h using a rotary mixer to obtain a homogenous mixture.

70 mg of the powder mixture was heated from ambient temperature to 620 °C at 2, 5, 10, 15 and 20 °C min^{-1} in a Simultaneous Thermal Analyzer (STA – Setaram SetsysEvo) to pinpoint the critical temperature, at which the thermochemical reaction between Mg and bredigite took place at its highest intensity (T_p), and possible mass change as a result of the exothermic reaction. The STA furnace was flushed with high purity argon gas for 4000 s. The STA tests were repeated three times for each heating rate.

Composite specimens were fabricated using a powder metallurgy method known as Pressure Assisted Sintering (PAS) (NaddafDezfuli et al., 2017b). In this method, the powder mixture was first heated to 350 °C in a 13 mm diameter die made from hot-work tool steel and then uniaxially compacted at 500 MPa. To ensure optimum densification of the PAS composite, the mixture was kept at 350 °C for 2 h under the compaction pressure. The PAS composite was then heated to 600 °C, which was close to the reaction peak temperature measured in the thermoanalytical tests. The thermal treatment was conducted in a tube furnace by heating the PAS composite to 500 °C at a heating rate of 5 °C min^{-1} and then from 500 to 600 °C at 1 °C min^{-1} to exercise more precise control over the heating process. An isothermal step of 1 h was followed, after the composite reached 600 °C, to allow diffusion to take place within and across Mg powder particles. The Thermally Treated (TT) composite was then cooled at 5 °C min^{-1} to room temperature. The thermal treatment was conducted under a protective atmosphere (high-purity argon). An illustration of the processing steps is given in

Fig. 1. The exposing surfaces of PAS and TT composite samples were ground by using 2400 grit SiC sandpaper, washed in an ultrasonic acetone bath for 3 min and then dried by an air blower.

2.2. Microstructure and chemical composition

The value of bulk density was determined using Archimedes' principle according to (ASTM B962 – 15, 2015). Microstructures and surface morphologies of the composite before and after the thermal treatment were characterized by using a high-resolution Digital Stereo Microscope (DSM, KEYENCE VHX-5000) and a Scanning Electron Microscope (SEM, JEOL-JSM-6500F) working at an accelerating voltage of 15.0 kV, which was equipped with an Energy Dispersive X-ray Spectroscope (EDS).

Phase identification of the composite before and after the thermal treatment was carried out by using a Bruker D8 Advance X-ray diffractometer with monochromatic Cu radiation (Kα1 λ = 0.154056 nm) over a 2θ-angle range between 10° and 130° and a step size of 0.020°. Semi-quantitative analysis was performed by scaling the intensities of the diffraction peaks from the sample to one diffraction peak intensity value of corundum (α-alumina). A Reference Intensity Ratio (RIR or I/Icor) was applied to each phase and the relative intensities compared to the I/Icor values were obtained from the ICDD-PDF4 database.

The chemical compositions of the surfaces of composite samples were determined by using a Fourier Transform Infrared Spectroscope (FTIR, Nicolet 6700 spectrometer, scan range 600–1300, three scans per sample) and an Energy Dispersive X-ray Spectroscope attached to the SEM microscope. Multiple point scanning and elemental mapping were carried out to determine the concentrations and distributions of elements in the surface layer.

2.3. Mechanical tests

The bulk mechanical properties of the composite were determined by performing compression tests at a crosshead speed of 0.5 mm/min in an INSTRON universal testing machine using a 50 kN load cell. The height-to-diameter ratio of specimens was one, according to (ASTM E9-09, 2009). The tests were stopped when the compressive load dropped by 20%.

The microhardness values of the composite before and after the thermal treatment were obtained from Vickers hardness test (Leica VMHT), using a square based pyramidal-shaped diamond indenter having an angle of 136° and at a dwelling time of 12 s, according to the standard test method (ASTM E384-99, 1999). Composite samples were indented at loads of 0.49, 1.96 and 9.8 N to evaluate the effect of indentation load on the mean value of microhardness. Indentation was repeated at least 15 times to ensure a reliable mean value. After indentation, the affected area was observed by using DSM.

2.4. In vitro degradation tests

2.4.1. Degradation in DMEM

Composite samples (13 mm diameter and height-to-diameter ratio of 1) were immersed in a HEPES buffered (25 mM) Dulbecco's modified Eagle's medium (DMEM - D1145, Sigma-Aldrich) at 37 °C for 1, 3, 6, 12, 24 and 30 days. An anti-bacterial and anti-fungus agent (A5955, Sigma-Aldrich) was added to DMEM by 1% to prevent bacterial and fungi from growth. The ratio of solution volume to surface area (SV/SA) was 30 mL/cm^2 according to ASTM G31-72. Degradation profiles of the composite before and after the thermal treatment were constructed by measuring the mass loss (%) of composite samples as a function of immersion time (day) in DMEM.

The composite specimens were washed in an ultrasonic acetone bath and then dried in air for 24 h after each immersion period. The chemical compositions of the surfaces of composite samples were determined using FTIR and EDAX according to Section 2.2. The mechanical properties of the dried specimens were evaluated by subjecting the specimens to compression tests, as described in subsection 2.3.

2.4.2. Electrochemical degradation

To evaluate the electrochemical behavior of composite samples, a three-electrode configuration was adopted to perform potentiodynamic polarization tests. A Saturated Calomel Electrode (SCE) was used as the reference electrode and a platinum mesh as the counter electrode. Prior to the potentiodynamic tests, Open Circuit Potential (OCP) measurements were performed during immersion up to 20 h using a Solartron 1250/1255 potentiostat. Cathodic polarization tests were carried out at an initial potential of - 0.2 V versus OCP increasing to 0.0 V versus OCP. Anodic polarization tests were carried out separately at an initial potential of 0.0 V versus OCP increasing to +0.5 V versus OCP. Both cathodic and anodic polarization tests were conducted at a scan rate of 1 mV/s in HEPES-buffered DMEM at 37 °C.

2.5. Biocompatibility and bioactivity assessments

2.5.1. Preparation of biomaterial extracts

For extraction, monolithic Mg and TT Mg-20 vol% bredigite samples with a diameter of 13 mm were cut into disks with a thickness of 2 mm and then the exposing surfaces were ground by 2400 grit SiC sandpaper. Subsequently, monolithic and composite disks were immersed in DMEM containing 10% fetal bovine serum with a surface area to volume ratio of 1.25 cm^2/mL and incubated in a humidified incubator at 37 °C and with 5% CO_2 for 24 and 72 h. The extracts were withdrawn and centrifuged at 1200 × *g* for 5 min at room temperature. The extracts were diluted with DMEM + 10% FBS + 1% penicillin/streptomycin at ratios of 1/4 and 1/16, and stored at 4 °C according to ISO 10993-12.

2.5.2. Indirect cell proliferation assay

MG-63 cells were adopted to evaluate the cytotoxicity of the composite (Zheng et al., 2010). The cell cytotoxicity of each extract sample was evaluated using 3-(4, 5-dimethylthiazol-2-yl)-2, 5-diphenyltetrazolium-bromide (MTT) assay. MG-63 cells were incubated in 96-well cell culture plates at a density 1 × 10^4 cells per well and incubated for 24 h. After incubation, the medium was replaced by the extracted medium and incubated for further 1, 6 and 12 days. The proliferation rate of cultured cells on each sample was compared with the tissue culture polystyrene plate (TCPS) as a control. After incubation with the extracts, the culture medium of each well was removed and 0.1 mL MTT solution (0.5 mg/mL, Sigma) added, followed by incubation for 4 h at 37 °C. The purple formazan crystals were dissolved by adding 0.1 mL Isopropanol (Sigma) per well on a shaking incubator for 15 min prior to absorbance measurement. The solutions of each well were transferred to 96-well plate and the optical density (OD) was recorded on a microplate reader (STAT FAX 2100, USA) at 545 nm. This assay was repeated five times and the final ODs normalized to the control OD.

2.5.3. Indirect cell differentiation assay

The differentiation behavior of MG-63 cells was evaluated by measuring ALP activity. Cells were cultured at a density of 1 × 10^4 cells/well in a 24-well plate for 24 h. Then the medium was replaced with the 24 and 72 h extracted media and incubated for further 3, 6 and 12 days. Subsequently, the cells in each well were lysed in 0.1% Triton X-100 (Sigma) and the lysates were incubated with p-nitrophenyl phosphate (pNPP) (Sigma) for 60 min at 37 °C. The quantity of p-nitrophenol produced was measured at 405 nm and the total protein content was acquired with the aid of a BCA Protein Assay Kit (Sigma). The results were expressed as nanomoles of p-nitrophenol produced per minute per microgram of protein. ALP activity of cells cultured in the medium supplemented with 10% FBS without any addition of extracts served as the control. At least five samples per each test were taken for statistical analysis. The statistical significance was defined as a *p*-value

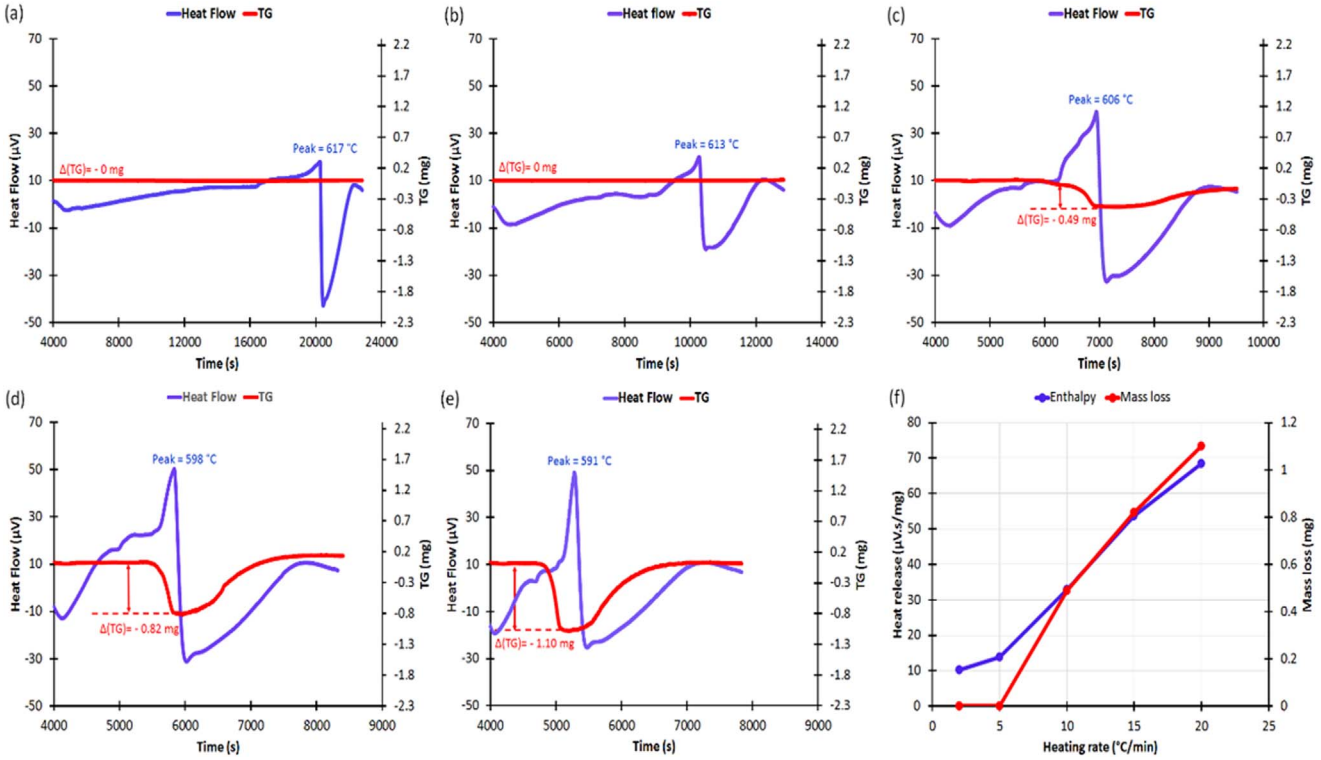

Fig. 2. Thermo-gravimetric profiles of Mg-20% bredigite samples heated to 620 °C at 2 (a), 5 (b), 10 (c), 15 (d) and 20 °C min^{-1} (e). Exothermic heat flow and mass loss as a function of heating rate (f).

of less than 0.05.

3. Results

3.1. Processing details and microstructure

Fig. 2 shows the thermal and gravimetric profiles of the Mg-20 vol% bredigite composite from room temperature to 620 °C, plotted by the data acquisition system of STA at 2, 5, 10, 15 and 20 °C min^{-1}. The heat flow curves of the composite revealed an exothermic event at all the heating rates (Fig. 2a-e). Surprisingly, the peak temperature of the reaction decreased with increasing heating rate. The amount of the generated heat increased by almost seven times when the heating rate was increased from 2 to 20 °C min^{-1} (Fig. 2f). Significant mass losses were observed in the TG curves when the composite was heated at relatively high heating rates (10, 15 and 20 °C).

Fig. 3 shows the optical microscopic images taken from the PAS composite after the thermal treatment (a-d), including SEM back-scattered micrographs and EDS elemental maps (e-h). The TT composite appeared to have a homogenous microstructure (Fig. 3a) with almost no pores or cracks throughout the material (Fig. 3b). A closer look at the microstructure of the etched TT composite (Fig. 3c with red arrows)

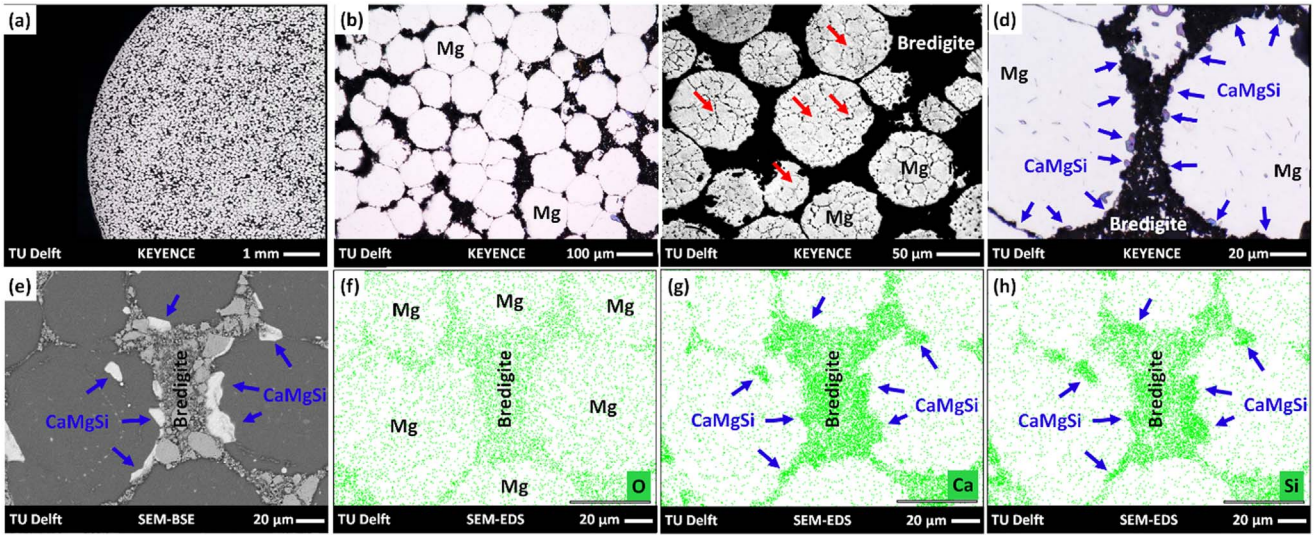

Fig. 3. Macroscopic and microscopic illustrations of the Mg-20% bredigite composite after the thermal treatment at 600 °C at different magnifications (a-d). Optical images of grain boundaries after etching (c – red arrows) and CaMgSi compound at the Mg-bredigite interface (d - blue arrows). SEM-BSE image of the TT composite (e) associated with EDS elemental distribution maps of oxygen (f), calcium (g) and silicon (h). (For interpretation of the references to color in this figure legend, the reader is referred to the web version of this article.).

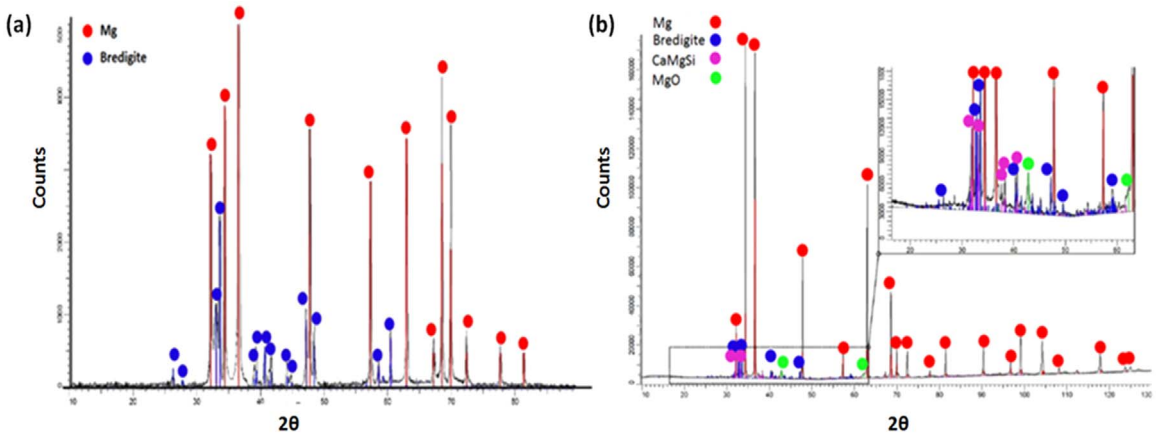

Fig. 4. XRD spectra of the Mg-20% bredigite composite before (a) and after (b) the thermal treatment at 600 °C.

revealed the grain structure of the Mg matrix with a mean grain size of approximately 10 μm.

After the thermal treatment, a newly formed interlayer at the Mg-bredigite interface was observed, appearing as a blue polygonal phase in the optical micrograph (Fig. 3d). This blue phase was also visible in the SEM-BSE image (Fig. 3e, indicated by blue arrows) having a strong contrast with the neighboring bredigite particles. EDS elemental mapping of the interface (Fig. 3f-h) showed the presence of Si and Ca in the interlayer between Mg and bredigite particles, indicating the diffusion of atoms from bredigite to this interlayer.

Fig. 4a and b shows the XRD spectra of composite samples before and after the thermal treatment. The X-ray reflections of the Mg matrix (red dots in Fig. 4) were assigned according to PDF 04-015-2580 and those of bredigite (blue dots in Fig. 4) were assigned according to PDF 00-036-0399. The crystal lattice of Mg was Hexagonal Close-Packed (HCP) and that of bredigite orthorhombic.

The XRD spectrum of the TT composite (Fig. 4b) contained the diffraction patterns of crystalline CaMgSi and MgO with relative amounts of 92 and 8 wt%, respectively. It confirmed that the blue-colored polygonal phase in light microscopy was in fact a CaMgSi intermetallic phase, present at the Mg-bredigite particle interface. The density of the PAS composite was increased by 2.1% (from 96.6% to 98.7%) as a result of the thermal treatment (Table 1).

3.2. Mechanical behavior

Fig. 5a illustrates the stress-strain curves of PAS and TT composite specimens in comparison with the curve of monolithic Mg. Superior mechanical behavior of the TT composite as compared to that of PAS and monolithic specimens was apparent. The Compressive Yield Strength (σ_{CYS}) of PAS specimens after the thermal treatment increased from 135.0 to 170.1 MPa, which represents a 26% improvement. The Ultimate Compressive Strength (σ_{UCS}) of the TT composite improved by 18% and 97%, relative to the values of PAS and monolithic specimens, respectively. The values of strain to fracture (ε_f), which represents bulk ductility, were 17.1%, 13.9% and 6.1% for TT, PAS and monolithic specimens, respectively.

The morphologies of specimens before the compression tests and after the failure are shown in Fig. 5b-d. Longitudinal cracks (Fig. 5c - red arrows) and surface delamination (Fig. 5c – black arrows) were the main characteristics of the PAS composite (NaddafDezfuli et al., 2017b). On TT specimens, however, no surface delamination was observed and longitudinal cracks were replaced by a 45° diagonal crack (Fig. 5d – yellow arrows).

Fig. 6a illustrates an overview of a representative crack on the cross section. Higher magnification images of the crack are given in Fig. 6b and d. Owing to the stronger Mg-bredigite interface, cracks (Fig. 6b, d - black arrows) propagated through the original Mg powder particles (yellow circle) rather than through the Mg-bredigite interface. Hence, the interface remained intact and inter-particle fracture was prohibited (Fig. 6d – green arrows). The second column of Fig. 6 shows relatively

Table 1
Bulk densities of monolithic Mg and Mg-20% bredigite composite before (PAS) and after the thermal treatment (TT) at 600 °C.

Material	Bulk density (vol%)
Mg	99.8% ± 0.2
Mg-20%Bredigite (PAS)	96.6% ± 0.7
Mg-20%Bredigite (TT)	98.7% ± 0.4

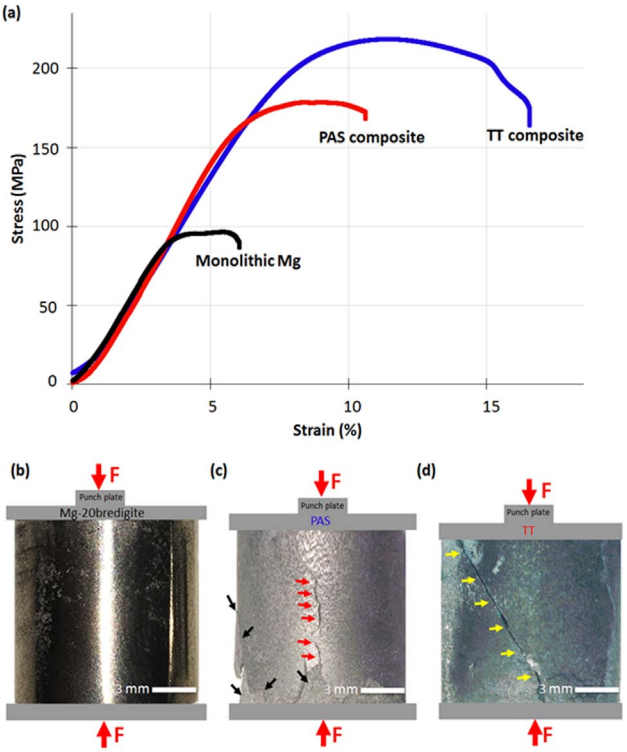

Fig. 5. Stress-strain curves of monolithic Mg, PAS and TT composite specimens (a). Bulk overview of Mg-20% bredigite composite specimen before the compression tests (b). Bulk overview of PAS (c) composite specimen after the compression tests, revealing longitudinal cracks (red arrows) and surface delamination (black arrows). Bulk overview of TT composite specimen after the compression test (d), revealing a 45° diagonal crack (yellow arrows). (For interpretation of the references to color in this figure legend, the reader is referred to the web version of this article.).

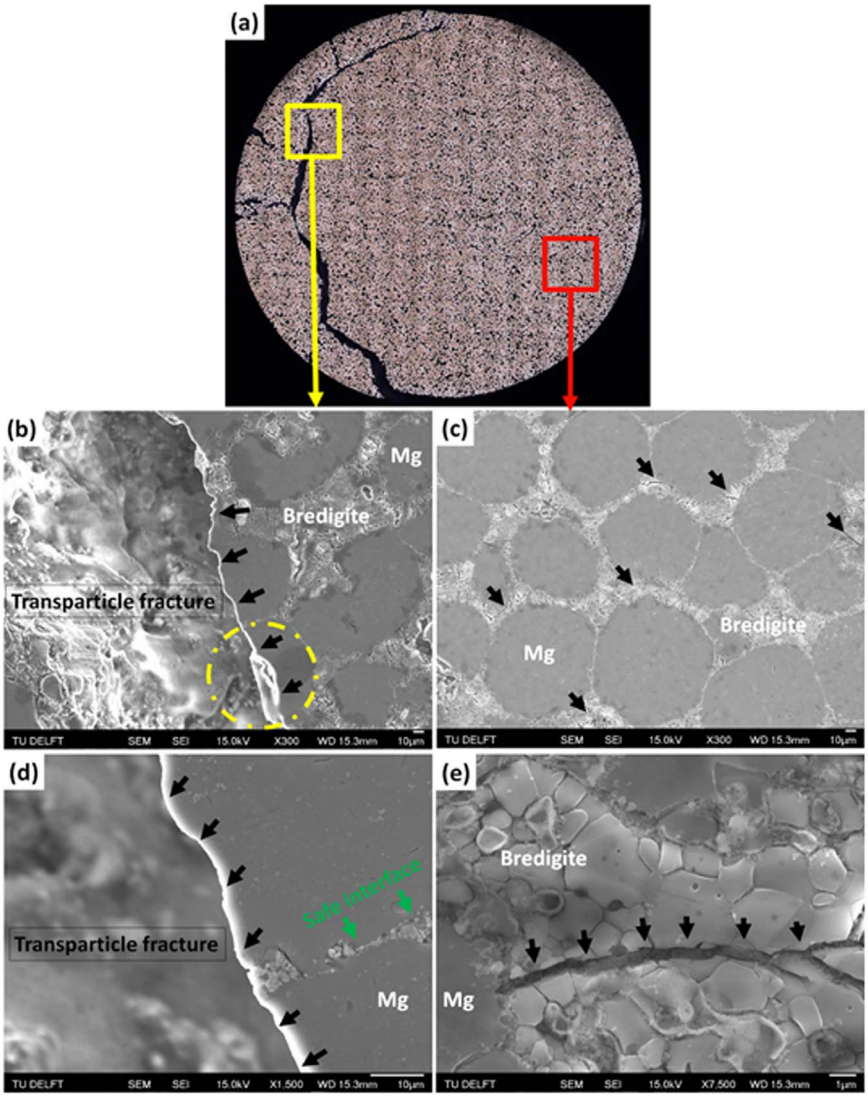

Fig. 6. Crack propagation pattern in a TT composite specimen (a) through Mg (first column) and bredigite (second column) original powder particles. Transparticle fracture through Mg (b, d – black arrows) and bredigite particles (c, e – black arrows) at different magnifications.

smaller cracks propagating through bredigite particles (Fig. 6c, e - black arrows) and being arrested when these cracks reached the metal-ceramic interface.

Fig. 7 shows the microstructure of the TT composite before and after indentation at different indentation loads. Increasing the indentation load from 0.49 to 9.80 N resulted in a larger value of microhardness, from 43.2 to 65.2 HV (Fig. 9a-d) and affected an increasing surface area of composite specimen (Fig. 7e-h), giving a better estimation of hardness on a larger scale. This is necessary since indenting specimens at different locations at the same load resulted in different values of microhardness (Fig. 7, second and third row). When the TT composite was indented at the Mg-bredigite interface, it resulted in a higher microhardness value (62.2 HV) as compared to the value when the composite was indented on an Mg particle surrounded by bredigite particles (54.7 HV).

Upon a closer look at the microstructure, large twinning bands were observed in the affected plastic deformation region, and their number appeared to be directly related to the applied load (black arrows in Fig. 7e-h).

The mechanical properties of the specimens and comparison to those of human bone are summarized in Table 2.

The microhardness values of the composite specimens were close to those of Mg-hydroxyapatite composites reported in (Witte et al., 2007b). On the other hand, the yield and ultimate compressive strengths of the TT composite were significantly higher than AZ91, Mg-hydroxyapatite, Mg-ßTCP and Mg-fluorapatite composites (Haghshenas, 2017)

3.3. In vitro biodegradation

Fig. 8a shows the mass loss profiles of PAS and TT Mg-20% bredigite composite samples as compared to the profile of monolithic Mg sample as a function of immersion time in DMEM. Fig. 8b shows the ultimate compressive strengths of specimens as a function of immersion time. The monolithic Mg specimens did not pass the test period of one month and were totally dissolved after 12 days of immersion. The average degradation rate of monolithic magnesium, i.e., 31.41 mg cm^{-2} day^{-1}, was in good agreement with that determined in previous studies on cast magnesium specimens (19–44 mg cm^{-2} day^{-1}) (Song, 2007). However, the PAS and thermally treated (TT) Mg-20% bredigite composites survived the test period of one month by dissolving at much slower rates than monolithic Mg. The thermal treatment considerably improved the degradation rate of the PAS composite (almost by 117%). The calculated amounts of mass loss, after one month immersion in DMEM, were 100%, 6.1% and 2.8%, equivalent to 31.41, 0.87, and 0.40 mg/cm^2/day for Mg, PAS and TT Mg-20% bredigite, respectively. The average

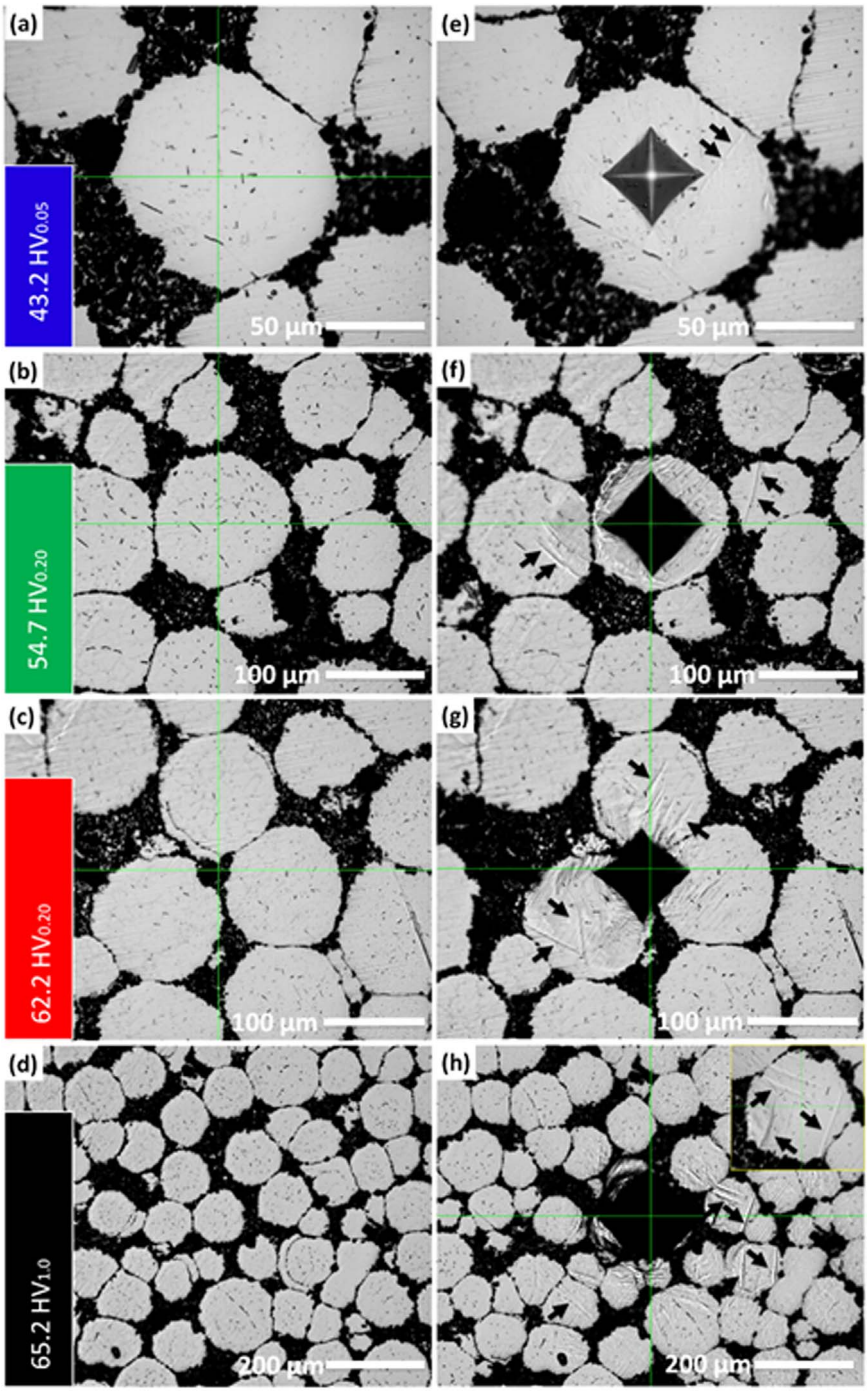

Fig. 7. Microstructures of the TT composite before (a-d) and after (e-h) indentation at $HV_{.05}$ (a, e), $HV_{.20}$ (b-c, f-g) and $HV_{1.0}$ (d, h), revealing large twin bands after the indentation (black arrows).

Table 2
Mechanical properties of monolithic, PAS and TT specimens as compared to those of cortical and cancellous bone.

Material	σ_{CYS} (MPa)	σ_{UCS} (MPa)	Microhardness ($HV_{1.0}$)	ε_f (%)
Mg	90.5 ± 13.8	114.2 ± 21.4	38.2 ± 0.1	6.1 ± 0.9
PAS composite	135.0 ± 7.8	190.3 ± 12.2	64.0 ± 5.8	13.9 ± 1.8
TT composite	170.1 ± 6.4	225.5 ± 5.3	65.2 ± 6.8	17.1 ± 1.7
Cancellous bone	2–12 (Hench, 1991; Hench and Wilson, 1993)	1.7–12.0 (Hench, 1991; Hench and Wilson, 1993; Hvid et al., 1983)	32.9 ± 6.6 (Dall'Ara et al., 2007)	1.1 ± 0.6 (Røhl et al., 1991)
Cortical bone	115.1 ± 16.4 (Mirzaali et al., 2016)	153.6 ± 21.6 (Mirzaali et al., 2016)	28–59 (Zwierzak et al., 2009)	1.1–2.1 (Witte et al., 2008)

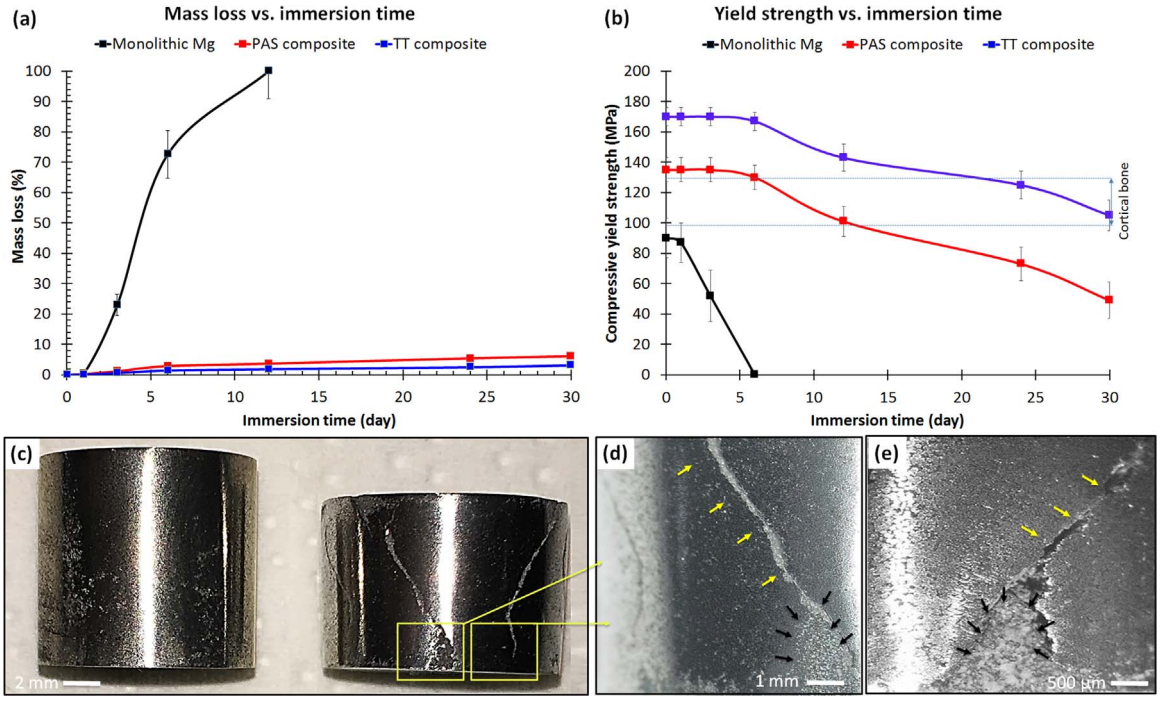

Fig. 8. Mass loss (a) and ultimate compressive strength (b) profiles of monolithic Mg and Mg-20% bredigite composite before (PAS) and after (TT) the thermal treatment as a function of immersion time. Optical micrographs of the TT composite subsequent to degradation tests and mechanical tests (c) with a magnified view (d, e) of localized corrosion (black arrows) and mechanical cracks (yellow arrows). (For interpretation of the references to color in this figure legend, the reader is referred to the web version of this article.).

degradation rate of TT composite was slightly higher than that of WE43 in 3.5% NaCl solution (0.26 mg cm^{-2} day^{-1}), and much lower than that of cast ZE41 and AZ91 alloys at average dissolution rates of 7.71 and 6.95 mg cm^{-2} day^{-1} in buffered Hank's solution, respectively (Song, 2007; Taltavull et al., 2014).

As a result of a lower degradation rate, the compressive yield strength of the TT composite remained within the strength range of cortical bone up to one month of immersion in DMEM (Fig. 8). On the other hand, the compressive yield strengths of monolithic and the PAS composite fell below the strength range of cortical bone within 12 days of immersion.

Localized corrosion was still the dominating degradation mechanism of the TT composite, initiating mostly from the bottom edges of the specimens (Fig. 8c-e yellow insets and black arrows). These localized corrosion features resulted in stress concentrations, facilitating the initiation of cracks when the material was under compressive loading, as shown in Fig. 8d and e (indicated by yellow arrows).

Fig. 9a shows the open circuit corrosion potentials (OCP) of monolithic Mg and Mg-20% bredigite composite before and after the heat treatment. The OCP potentials of samples first increased to more positive values and then gradually reached a steady state where the OCP potentials remained relatively constant. The TT composite showed a higher OCP value after 20 h immersion. In the PDP curves, the TT composite showed a mild shift towards higher cathodic activities with respect to the PAS specimen (Fig. 9b). It was difficult to judge the general anodic activity of the TT composite with respect to that of the PAS composite, because it was marginally shifting below and above that of the PAS composite during the polarization test (Fig. 9C).

3.4. Morphology and chemistry of the corrosion product layer

Fig. 10 shows the SEM micrographs taken from the TT composite after 1, 3, 6, 12, 24, and 30 days of immersion in DMEM. The surface layer after 1-day immersion revealed an integrated network of large cracks surrounding original Mg powder particles (Fig. 10a - black arrows). After three days, a second layer started to form on top of the first layer and the former contained smaller cracks, which posed a slightly lighter contrast with respect to the first layer under backscattered electron imaging (Fig. 10b-f – yellow arrows). Localized corrosion initiated during the first day of immersion, mostly at the bottom edges of specimens where the material was in direct contact with the die during processing, and further expanded over the edges as immersion time increased from 3 to 30 days (Fig. 10 – insets).

The SEM back-scattered micrographs at higher magnifications

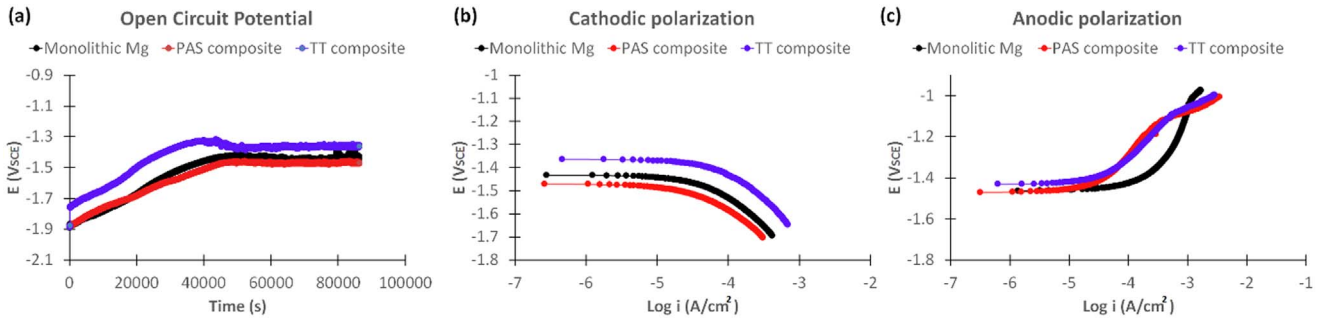

Fig. 9. OCP (a), cathodic (b) and anodic polarization (c) curves of the Mg-20% bredigite composite before (PAS composite) and after the heat treatment (TT composite).

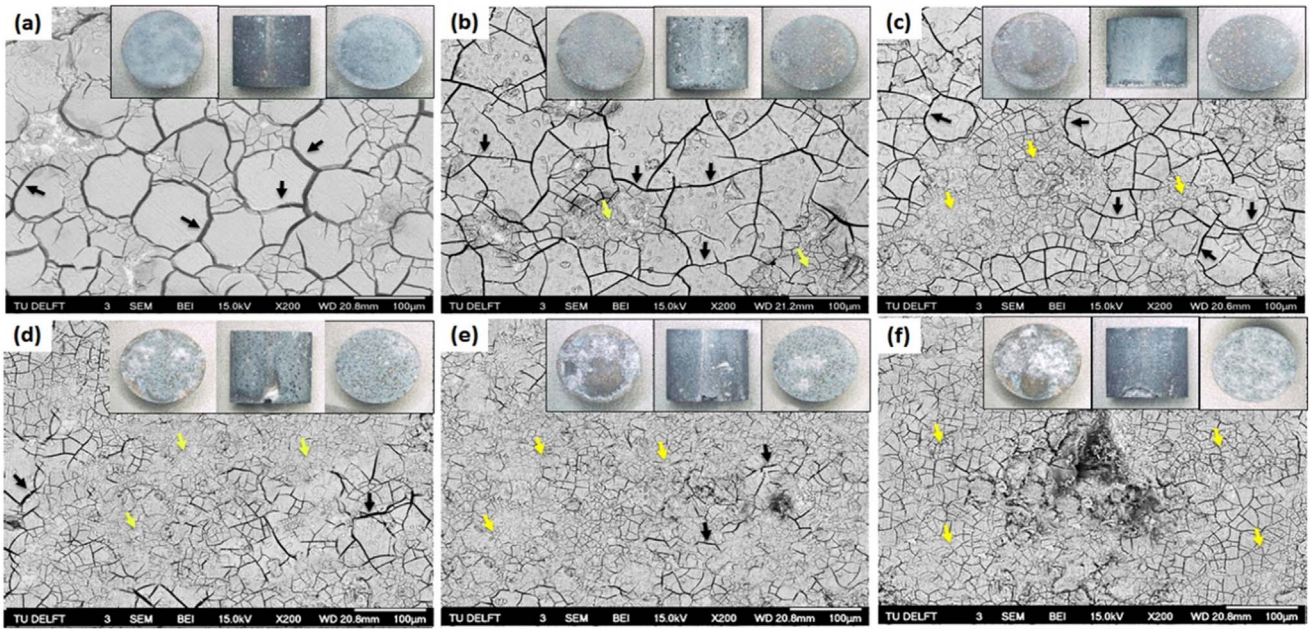

Fig. 10. SEM micrographs of the thermally treated Mg-20% bredigite composite after immersion in DMEM solution for 1 (a), 3 (b), 6 (c), 12 (d), 24 (e) and 30 (f) days, showing large cracks within the initial layer (black arrows) and relatively smaller cracks within the second layer (yellow arrows). The insets represent the bottom, front and top view of corroded samples, from left to right, respectively. (For interpretation of the references to color in this figure legend, the reader is referred to the web version of this article.).

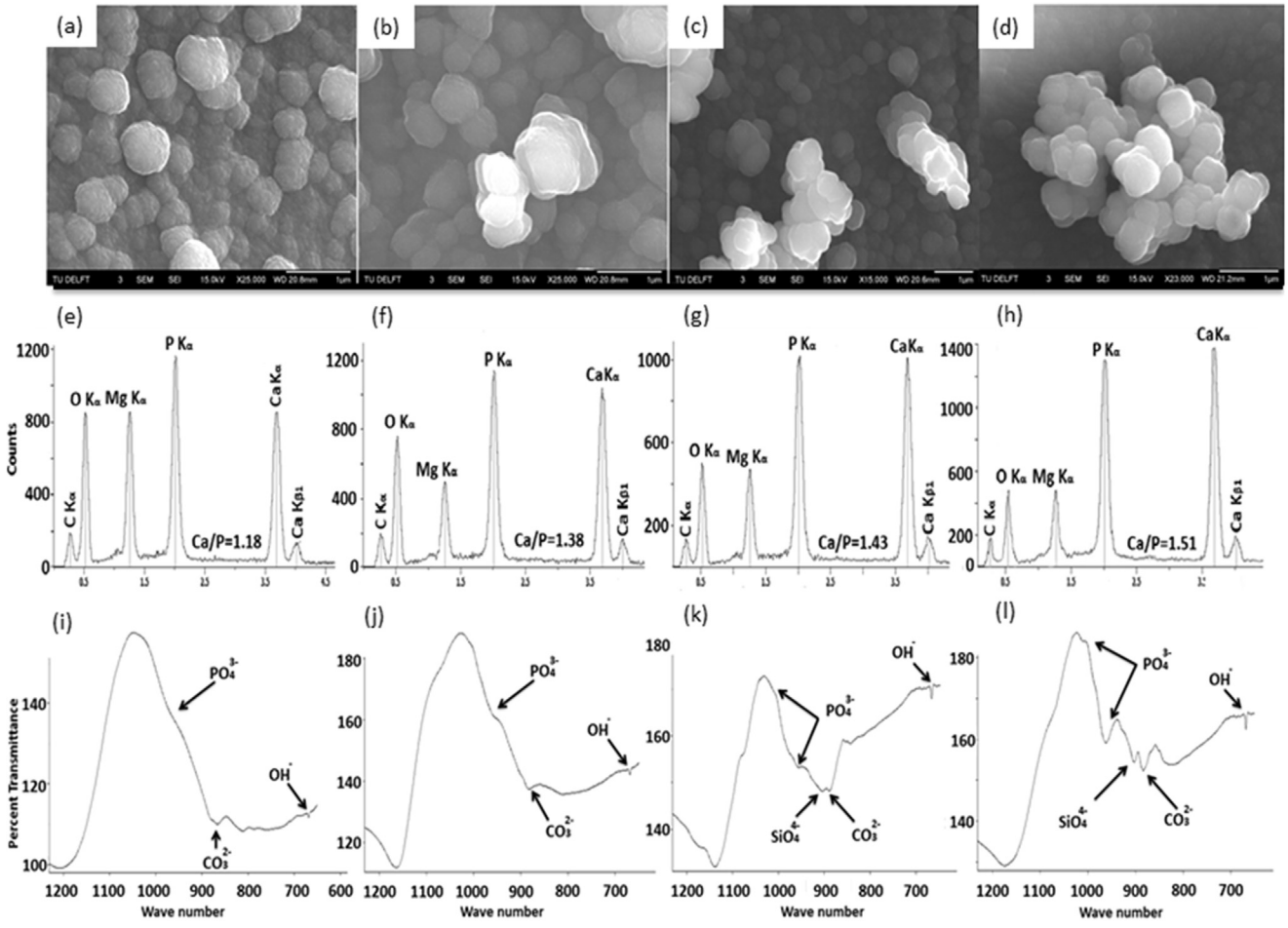

Fig. 11. Surface morphologies (a-d), EDS point scans (e-h) and FTIR spectra (i-l) of the thermally treated Mg-20% bredigite composite after 1 (1st column), 3 (2nd column), 6 (3rd column) and 12 (4th column) day immersion.

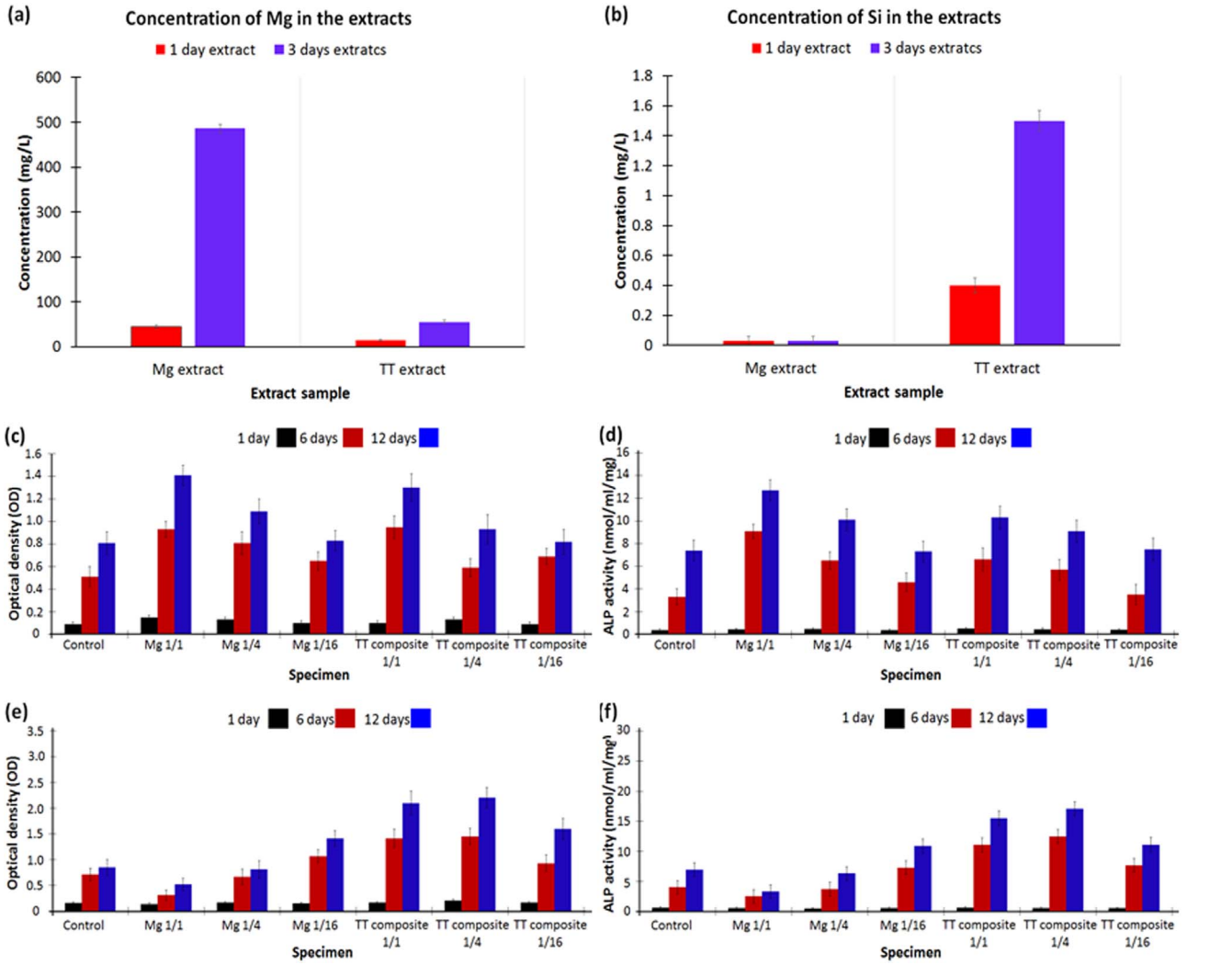

Fig. 12. Concentrations of Mg (a) and Si (b) ions in the original Mg and TT composite extracts after 1 and 3 days of extraction. MTT (a and c) and ALP assays (b and d) of MG-63 cells in 1-day (first row) and 3-day (second row) monolithic and TT composite extracts at different dilution ratios.

(Fig. 11a-d) showed that after one-day immersion, the surface layer was composed of submicron spherical agglomerates, being tightly bonded with each other and protecting the substrate from extensive dissolution. This initial compact layer also acted as a substrate for further heterogeneous nucleation of agglomerates. The sizes of spheres were about 500 nm and they precipitated on top of each other, forming larger agglomerates (Fig. 11b-d). The second layer of agglomerates was more porous and had less magnesium incorporated into its structure, which caused the Ca/P ratio of the surface layer to increase from 1.18 to 1.51 at day 12 (Fig. 11e-h).

Our results show that after one-day immersion, the protective surface layer on the TT composite was mainly composed of O, C, Mg, Ca, and P (Fig. 11e-h). The Ca/P ratio of the surface layer (1.18) was lower than the stoichiometric value of hydroxyapatite (HA, 1.67), indicating that the surface layer was deficient in calcium. The FTIR spectra of the same surface (Fig. 11i-l) showed absorption bands of carbonate, phosphate and a low intensity band of HA hydroxyl ions (Ślósarczyk et al., 2005), indicating the early formation of magnesium-containing hydroxyl-carbonate apatite precipitates. The absorption bands of silica appeared at day 6 and became more distinguishable from those of carbonate at day 12.

3.5. Cytotoxicity and bioactivity

Fig. 12a and b shows the elemental concentrations of Mg and Si in the original 1- and 3-day extracts of monolithic Mg and TT composite samples. The concentration of Mg in the original Mg extracts increased by 441 mg/L in 3-day extraction while that of Mg in the original TT composite extracts increased only by 40 mg/L. On the other hand, the amount of Si in the original TT extracts remained below 2 mg/L after 3-day extraction, revealing limited participation of Si in the original TT composite extracts.

The results of the MTT assay (Fig. 12c) revealed similar optical densities for the extracts of Mg and Mg-20% Bredigite TT composite after one day of immersion. After 6 and 12 days of incubation, the density of the MG-63 cells in the Mg original extract (concentration of Mg = 45 mg/L) was still slightly higher than that of cells in the TT composite extract (concentration of Mg = 14 mg/L), indicating that cells in the original 1-day Mg extracts were more viable. When the original 1-day extracts were diluted by 1/4 and 1/16, the cell viability values of the control, monolithic Mg and the TT composite were almost the same with no statically significant differences, which means that the viability was dominated by the concentration of Mg ions in the extracts. The 3-day extraction period gave enough time to Mg and bredigite particles at the exposing surface to react with the solution, which resulted in higher concentrations of Mg and Si ions in DMEM. As a result, the 3-day Mg original extracts (concentration of Mg i = 486 mg/L) were cytotoxic from the beginning throughout the testing period (Fig. 12). At day 3, the viability of MG-63 cells and their density in the original extracts of the TT composite were higher than those in the Mg

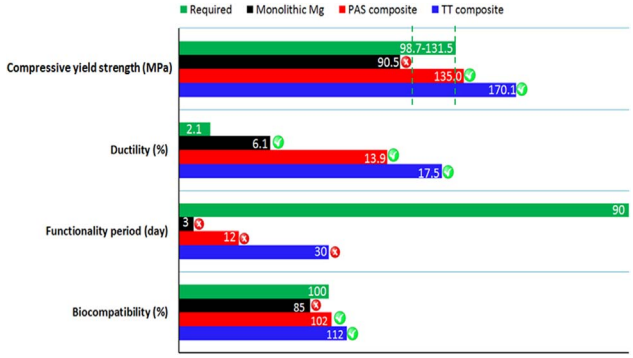

Fig. 13. Mechanical properties, degradation and biocompatibility of the PAS and TT Mg-bredigite composite compared to the minimum requirements for meaningful long-term in-vivo tests.

group and also the control group, indicating the stimulatory effect of the composite extracts on the proliferation of MG-63 cells (Fig. 12). The same as the 1-day extracts, 1/16 dilution of the original extracts resulted in similar viability levels for all the samples, showing once again that the viability of cells in contact with the extracts was closely related to the concentrations of ionic products, particularly Mg and Si ions in the DMEM solution.

The alkaline phosphatase activity of MG-63 cells in response to 1-day and 3-day extracts resembled the trend of viability assays (Fig. 12d, f). MG-63 cell differentiation in the 1-day original Mg extracts was higher than the control, although cell differentiation was obviously limited in 3-day Mg original extracts. On the other hand, the TT composite showed no sign of limited differentiation in its extracts. Similar to the MTT tests, diluting the extract by 1/16 overshadowed the effect of corrosion products on cell proliferation, resulting in a similar extent of cell proliferation for monolithic and TT composite samples.

Fig. 13 illustrates the mechanical properties, mechanical functionality period and biocompatibility of the PAS and TT composite as compared to the minimum requirements for meaningful long-term in-vivo tests. It shows that to prepare the TT composite for meaningful long-term in-vivo tests, the period of the mechanical functionality in DMEM should be further extended to at least 3 months in order to allow full recovery of damaged bone before the composite loses its role as a mechanical support.

4. Discussion

The exothermic reaction between bredigite and Mg resembles the reaction between Mg and SiO_2 particles, because the atomic configuration of Si-O in bredigite is identical to that of the monolithic SiO_2 (Umeda et al., 2009). Both form tetrahedrons with Si atoms in the center, and oxygen atoms at the corner of the tetrahedrons. The only difference is that in SiO_2, bridging oxygen atoms at the corner of a tetrahedron are connected to another Si atom in the adjacent tetrahedron, while in the bioceramics the bridging O atoms could be connected to Mg and Ca atoms (Carbonneau et al., 1998; Eisenmann et al., 1972). The Mg–O bonds in the bioceramic form an octahedron structure with Mg atoms at the center and six bridging oxygen atoms at the corners of tetrahedrons (Lee et al., 2012). Each chain of tetrahedrons is connected to an adjacent octahedral layer (Mg octahedrons) by a bridging oxygen, producing a structure of alternating tetrahedral-octahedral-tetrahedral (T-O-T) layers. Calcium atoms connect the alternate T-O-T layers together with a coordination number of 8. Thus, three types of atomic bonding, namely Si–O–Si, Si–O–Mg and Si–O–Ca, coexist in the crystal structure of bredigite. Practically, there are only two types of atomic bonds, namely Si–O–Si and Si–O–Ca that can be broken by Mg because magnesium cannot reduce its own oxide. Since dissociation of Si–O bonds during the solid-state exothermic reaction would release a larger amount of energy due to the higher bond dissociation energy of Si–O bonds, compared to that of Ca–O bonds (Christian, 1973; Sanderson, 2012), its bonding energy will dominate the amount of energy that is released during the exothermic reaction (Fig. 2). The thermal dissociation of bredigite could be initiated through a reaction between Mg and Si–O–Si and Si–O–Ca bonds, in which Mg removes the bridging oxygen and oxidizes into MgO, exposing elemental Si and Ca to the interface and producing CaMgSi and MgO at the interface, which could be simplified as:

$16Mg + Ca_7MgSi_4O_{16} \rightarrow 16MgO + 4Si + 7Ca + Mg$ Reduction of bredigite (reaction 1)

$Mg + Si + Ca \rightarrow CaMgSi$ Product formation (reaction 2)

Some intermediate products could also form during the thermal dissociation of bredigite, which would make reaction 1 and 2 more complex. This could be clarified by means of in-situ high temperature X-day diffraction. According to the ternary phase diagram of Ca-Mg-Si (Gröbner et al., 2003), if diffusion is allowed to take place, then the formation of CaMgSi above 400 °C would be possible when Ca atoms are added at the expense of Mg atoms in the structure of Mg_2Si to an equal atomic fraction of 33.33%. The structural similarity of bredigite to CaMgSi may also assist in the formation of the CaMgSi compound at the interface, because both have an orthorhombic crystal structure (Carbonneau et al., 1998).

This CaMgSi layer allows diffusion through the Mg-bredigite interface (Fig. 3f-h), developing a much stronger and more integrated Mg-bredigite particle interface compared to that in the PAS composite (Fig. 5). The thermal treatment has a second benefit, i.e., the strengthening of Mg-Mg particle bonds through inter-particle diffusion. The PAS composite has a better chance to be sintered than original powder particles because the oxide layer on Mg powder particles is disrupted by large plastic deformation of Mg particles during PAS (NaddafDezfuli et al., 2017b).

The in-situ fabrication of TT composites is a delicate process and thus requires careful control over the heating process. It was shown that when the composite was heated at a relatively fast heating rate (10, 15 and 20 °C min^{-1}), the exothermic reaction between Mg and bredigite particles took place at a much higher intensity, which generated a larger amount of heat at a short time (Fig. 2), resulting in significant mass loss which could cause the evaporation of Mg particles (NaddafDezfuli et al., 2017b). On the other hand, the TG curves at lower heating rates (< 5 °C min^{-1}) revealed no evidence of possible mass loss during the exothermic reaction. In this research, the solid-state reaction between Mg and bredigite was successfully triggered while overcoming the issue of local evaporation of the Mg matrix (NaddafDezfuli et al., 2017b) by heating the composites at 1 °C min^{-1}. The reasons for the strong influence of heating rate on the reaction peak temperature and on the amount of heat released from the exothermic reaction are not clear and it requires a thorough thermoanalytical study which is out of the scope of this research.

A stronger particle interface in the TT composite resolved the issue of a lack of load transfer from the matrix to ceramic particles and cracks deviated from powder particle interfaces to the interior of Mg and bredigite particles, shifting the failure mode from *inter-particle* fracture to *trans-particle* fracture (Fig. 6) during compression testing. As a result, pre-mature inter-particle fracture and surface delamination, which are often associated with metal matrix composites (Luo, 1995; NaddafDezfuli et al., 2017b), were prohibited, resulting in 26% and 18% improvements in yield and ultimate compressive strengths, respectively (Table 2).

The difficulty of cross slip in HCP magnesium and the higher critical resolved shear stress (CRSS) required for the < c + a > slip (40 MPa) than for twining (2–3 MPa) (Mahdavian et al., 2013; Reed-Hill and Robertson, 1957) reduce the ability of the material to deform by dislocation slip, and thus deformation twinning occurs (Fig. 7). However,

the presence of micro-sized bredigite particles in the composite may activate non-basal dislocations necessary for the ductile behavior of the Mg matrix (NaddafDezfuli et al., 2017b; Reihanian et al., 2014). This explains the enhanced strains of the composite obtained from the compression tests, in comparison with monolithic magnesium.

When TT composite specimens were immersed in the DMEM solution, surface cracks developed (Fig. 10) as a consequence of grain/powder particle boundary dissolution caused by high energy domains of dislocations at grain boundaries (Andrei et al., 2002), which activated the anodic dissolution of the adjacent Mg matrix (NaddafDezfuli et al., 2014). They provided pathways for fresh DMEM to reach the unreacted part of the substrate and thereby encouraging further dissolution of the matrix, leading to the accumulation of magnesium cations close to the corroding surface. Accumulation of Mg^{2+} cations close to the corroding surface encouraged the formation of a $Mg(OH)_2$ layer, with incorporation of Ca and P into this layer later (Fig. 11). The early submicron magnesium-containing hydroxyl-carbonate apatite precipitates, shown in Fig. 11a-d, were deficient in calcium, resembling the biological HA, which is also deficient in calcium (Lu et al., 2012). The hydroxyl-carbonate apatite phase is chemically and structurally equivalent to the mineral phase in bone, which is responsible for the bonding of bone tissue with the implant (Hench, 1991; Kannan, 2015). After 1-day immersion, more incorporation of Ca into HA crystals took place at the expense of Mg (Fig. 11e-h), owing to the better protection of the surface after one-day immersion and thus a smaller amount of Mg^{2+} became available around the corroding surface. Silicon from bredigite or CaMgSi was detected in the chemistry of the surface layer only after day 6 (Fig. 11k and l). One reason for relatively low silicon involvement is that calcium ions from bredigite were released preferentially to silicon ions by ion exchange with H^+ (Liu et al., 2004). Thus, most of silicone in bredigite would stay within the unreacted part (Hu et al., 2011), forming a negatively charged surface with the functional group ($\equiv Si - O^-$) (Liu et al., 2004).

Localized corrosion of the Mg matrix eventually resulted in the accumulation of magnesium cations in the vicinity of the corroding surface, which could be hydrolyzed by water, producing H^+ and acidifying the microenvironment (NaddafDezfuli et al., 2014). High concentration of H^+ discouraged the formation of a protective layer over the Mg matrix, which resulted in progressive local corrosion (NaddafDezfuli et al., 2014; Song and Atrens, 1999). The role of bredigite particles in blocking the progressive local corrosion sites in the Mg matrix was due to a relatively lower degradation rate of bredigite particles with respect to Mg (NaddafDezfuli et al., 2017b) and more importantly, due to the consumption of an excess amount of H^+ ion inside a corrosion pit (Dixit and Carroll, 2007) through ion exchange by either magnesium or calcium (Dixit and Carroll, 2007; Hench, 1991). The CaMgSi interlayer could also assist bredigite in blocking the corrosion pathways by consuming H^+ ions, similar to bredigite (Hagihara et al., 2013), although its role in balancing the pH might be negligible, considering its limited surface area with respect to bredigite particles. As a result of slower degradation, the mechanical properties of the TT composite remained within the strength range of cortical bone for nearly a month after immersion, which outperformed monolithic and PAS specimens (Fig. 8). The original extracts were proven to be stimulatory to the proliferation and differentiation of MG-63 cells (Fig. 12).

However, as Illustrated in Fig. 13, the period of the mechanical functionality in DMEM should be further extended to at least 3 months in order to prepare the TT composite for a meaningful long-term in-vivo test.

One effective way to gain more control over the localized corrosion at the edges of specimens would be to limit, or in an ideal case, totally prevent the development of friction between the outer layer of composite specimen and the die during compaction. In this way, the material close to the edges of the specimen could move freely during compaction, enhancing the integrity of the microstructure particularly around the edges. Examples of possible useful fabrication methods would be Acoustic Levitation (AL) and Hot Isostatic Pressing (HIP) (Carreño-Morelli et al., 2004; Scholz et al., 2014).

5. Conclusions

The in-situ fabrication of the Mg-20%bredigite composite was proven to be a feasible method to achieve homogeneity and integration in microstructure, mechanical compatibility to human bone, controlled degradation rate, cytocompatibility and bioactivity at the same time. It was found that the mechanical properties of the Mg-20%bredigite composite were significantly affected by the bonding strength of the composite constituents. The bonding strength of the Mg-bredigite interface was improved by triggering a solid-state exothermic reaction between Mg and bredigite particles, developing a CaMgSi intermetallic compound at the interface and enabling chemical interlocking at particle interfaces through diffusion across the CaMgSi interlayer.

The mechanical properties of the composite after the thermal treatment were comparable with those of human bone, outperforming monolithic and PAS specimens in strength and ductility. It shows that further improving the mechanical properties of the TT composite for orthopedic applications would not be necessary, although it is still possible if needed.

On the other hand, the degradation rate of the TT composite, particularly due to the localized corrosion, should be limited further to preserve the mechanical functionality of the composite for a longer period of time. Further research should be directed towards improving the degradation behavior of the TT composite by either removing susceptible areas for degradation in the microstructure, or by protecting the surface with a compact biodegradable surface layer to delay the degradation of the substrate.

Acknowledgements

This work was supported by the Netherlands Organization for Health Research and Development (ZonMw) under the project 1163500004.

References

Alvarez-Lopez, M., Pereda, M.D., Del Valle, J., Fernandez-Lorenzo, M., Garcia-Alonso, M., Ruano, O.A., Escudero, M., 2010. Corrosion behaviour of AZ31 magnesium alloy with different grain sizes in simulated biological fluids. Acta Biomater. 6, 1763–1771.

Andrei, M., Eliezer, A., Bonora, P.L., Gutman, E.M., 2002. DC and AC polarisation study on magnesium alloys Influence of the mechanical deformation. Mater. Corros. 53, 455–461.

Askeland, D.R., Phulé, P.P., 2003. The science and engineering of materials.

Carbonneau, Y., Couture, A., Van Neste, A., Tremblay, R., 1998. On the observation of a new ternary MgSiCa phase in Mg-Si alloys. Metall. Mater. Trans. A 29, 1759–1763.

Carreño-Morelli, E., Yang, J., Couteau, E., Hernadi, K., Seo, J.W., Bonjour, C., Forró, L., Schaller, R., 2004. Carbon nanotube/magnesium composites. Phys. Status Solidi (a) 201, R53–R55.

Christian, J.D., 1973. Strength of chemical bonds. J. Chem. Educ. 50, 176.

Dall'Ara, E., Öhman, C., Baleani, M., Viceconti, M., 2007. The effect of tissue condition and applied load on Vickers hardness of human trabecular bone. J. Biomech. 40, 3267–3270.

Dixit, S., Carroll, S.A., 2007. Effect of solution saturation state and temperature on diopside dissolution. Geochem. Trans. 8, 3.

Eisenmann, B., Schäfer, H., Weiss, A., 1972. Der Übergang vom "geordneten" anti-PbCl2-gitter zum anti-PbFCl-gitter: ternäre phasen ABX der erdalkalimetalle mit elementen der 4. Hauptgruppe (A = Ca, Sr, Ba; B = Mg; X = Si, Ge, Sn, Pb). Z. Anorg. Allg. Chem. 391, 241–254.

Gröbner, J., Chumak, I., Schmid-Fetzer, R., 2003. Experimental study of ternary Ca–Mg–Si phase equilibria and thermodynamic assessment of Ca–Si and Ca–Mg–Si systems. Intermetallics 11, 1065–1074.

Gu, X., Zhou, W., Zheng, Y., Dong, L., Xi, Y., Chai, D., 2010. Microstructure, mechanical property, bio-corrosion and cytotoxicity evaluations of Mg/HA composites. Mater. Sci. Eng.: C 30, 827–832.

Haghshenas, M., Mechanical characteristics of biodegradable magnesium matrix composites: a review. J. Magn. Alloy., 5, 2017, pp. 189–201.

Hagihara, K., Fujii, K., Matsugaki, A., Nakano, T., 2013. Possibility of Mg- and Ca-based intermetallic compounds as new biodegradable implant materials. Mater. Sci. Eng.: C 33, 4101–4111.

Hench, L.L., 1991. Bioceramics: from concept to clinic. J. Am. Ceram. Soc. 74, 1487–1510.
Hench, L.L., Wilson, J., 1993. An Introduction to Bioceramics. World Scientific, London.
Hong, D., Saha, P., Chou, D.-T., Lee, B., Collins, B.E., Tan, Z., Dong, Z., Kumta, P.N., 2013. In vitro degradation and cytotoxicity response of Mg–4% Zn–0.5% Zr (ZK40) alloy as a potential biodegradable material. Acta Biomater. 9, 8534–8547.
Hu, S., Zhang, R., Zhang, X., 2011. Study on mineral surface reacted with water at temperatures above 300 °C and 23 MPa. Res. Chem. Intermed. 37, 503–514.
Hvid, I., Christensen, P., Søndergaard, J., Christensen, P.B., Larsen, C.G., 1983. Compressive strength of tibial cancellous bone: instron® and osteopenetrometer measurements in an autopsy material. Acta Orthop. Scand. 54, 819–825.
Kannan, M.B., 2015. 13 - Hydroxyapatite Coating on Biodegradable Magnesium and Magnesium-Based Alloys A2 - Mucalo, Michael, Hydroxyapatite (Hap) for Biomedical Applications. Woodhead Publishing, pp. 289–306.
Kondoh, K., Oginuma, H., Kimura, A., Matsukawa, S., Aizawa, T., 2003. In-situ synthesis of Mg2Si intermetallics via powder metallurgy process. Mater. Trans. 44, 981–985.
Kulekci, M.K., 2008. Magnesium and its alloys applications in automotive industry. Int. J. Adv. Manuf. Technol. 39, 851–865.
Lee, K.H., Park, S.H., Yoon, H.S., Kim, Y.-I., Jang, H.G., Im, W.B., 2012. Bredigite-structure orthosilicate phosphor as a green component for white LED: the structural and optical properties. Opt. Express 20, 6248–6257.
Liu, C., Xin, Y., Tang, G., Chu, P.K., 2007. Influence of heat treatment on degradation behavior of bio-degradable die-cast AZ63 magnesium alloy in simulated body fluid. Mater. Sci. Eng.: A 456, 350–357.
Liu, X., Ding, C., Chu, P.K., 2004. Mechanism of apatite formation on wollastonite coatings in simulated body fluids. Biomaterials 25, 1755–1761.
Lu, W., Chen, Z., Huang, P., Yan, P., Yan, B., 2012. Microstructure, corrosion resistance and biocompatibility of biomimetic HA-Based Ca-P coatings on ZK60 magnesium alloy. Int. J. Electrochem. Sci. 7, 12668–12679.
Luo, A., 1995. Processing, microstructure, and mechanical behavior of cast magnesium metal matrix composites. Metall. Mater. Trans. A 26, 2445–2455.
Luo, A.A., 2013. Magnesium casting technology for structural applications. J. Magnes. Alloy. 1, 2–22.
Mahdavian, M.M., Ghalandari, L., Reihanian, M., 2013. Accumulative roll bonding of multilayered Cu/Zn/Al: an evaluation of microstructure and mechanical properties. Mater. Sci. Eng.: A 579, 99–107.
Mirzaali, M.J., Schwiedrzik, J.J., Thaiwichai, S., Best, J.P., Michler, J., Zysset, P.K., Wolfram, U., 2016. Mechanical properties of cortical bone and their relationships with age, gender, composition and microindentation properties in the elderly. Bone 93, 196–211.
NaddafDezfuli, S., Huan, Z., Mol, A., Leeflang, S., Chang, J., Zhou, J., 2017a. Advanced bredigite-containing magnesium-matrix composites for biodegradable bone implant applications. Mater. Sci. Eng.: C 79, 647–660.
NaddafDezfuli, S., Huan, Z., Mol, J.M.C., Leeflang, M.A., Chang, J., Zhou, J., 2014. Influence of HEPES buffer on the local pH and formation of surface layer during in vitro degradation tests of magnesium in DMEM. Prog. Nat. Sci.: Mater. Int. 24, 531–538.
NaddafDezfuli, S., Leeflang, S., Chang, J., Zhou, J., 2017b. Fabrication of novel magnesium-matrix composites and their mechanical properties prior to and during in vitro degradation. J. Mech. Behav. Biomed. Mater. 67, 74–86.
NaddafDezfuli, S., Sadrnezhaad, S.K., Shokrgozar, M.A., Bonakdar, S., 2012. Fabrication of biocompatible titanium scaffolds using space holder technique. J. Mater. Sci. Mater. Med. 23, 2483–2488.
Reed-Hill, R.E., Robertson, W.D., 1957. Additional modes of deformation twinning in magnesium. Acta Metall. 5, 717–727.
Reihanian, M., Hadadian, F.K., Paydar, M.H., 2014. Fabrication of Al–2 vol% Al2O3/SiC hybrid composite via accumulative roll bonding (ARB): an investigation of the microstructure and mechanical properties. Mater. Sci. Eng.: A 607, 188–196.
Røhl, L., Larsen, E., Linde, F., Odgaard, A., Jørgensen, J., 1991. Tensile and compressive properties of cancellous bone. J. Biomech. 24, 1143–1149.
Sanderson, R., 2012. Chemical Bonds and Bonds Energy. Elsevier.
Scholz, M.S., Drinkwater, B.W., Trask, R.S., 2014. Ultrasonic assembly of anisotropic short fibre reinforced composites. Ultrasonics 54, 1015–1019.
Ślósarczyk, A., Paszkiewicz, Z., Paluszkiewicz, C., 2005. FTIR and XRD evaluation of carbonated hydroxyapatite powders synthesized by wet methods. J. Mol. Struct. 744, 657–661.
Song, G., 2007. Control of biodegradation of biocompatable magnesium alloys. Corros. Sci. 49, 1696–1701.
Song, G.L., Atrens, A., 1999. Corrosion mechanisms of magnesium alloys. Adv. Eng. Mater. 1, 11–33.
Staiger, M.P., Pietak, A.M., Huadmai, J., Dias, G., 2006. Magnesium and its alloys as orthopedic biomaterials: a review. Biomaterials 27, 1728–1734.
Taltavull, C., Shi, Z., Torres, B., Rams, J., Atrens, A., 2014. Influence of the chloride ion concentration on the corrosion of high-purity Mg, ZE41 and AZ91 in buffered Hank's solution. J. Mater. Sci.: Mater. Med. 25, 329–345.
Umeda, J., Kondoh, K., Kawakami, M., Imai, H., 2009. Powder metallurgy magnesium composite with magnesium silicide in using rice husk silica particles. Powder Technol. 189, 399–403.
Witte, F., 2010. The history of biodegradable magnesium implants: a review. Acta Biomater. 6, 1680–1692.
Witte, F., Feyerabend, F., Maier, P., Fischer, J., Stormer, M., Blawert, C., Dietzel, W., Hort, N., 2007a. Biodegradable magnesium-hydroxyapatite metal matrix composites. Biomaterials 28, 2163–2174.
Witte, F., Feyerabend, F., Maier, P., Fischer, J., Störmer, M., Blawert, C., Dietzel, W., Hort, N., 2007b. Biodegradable magnesium–hydroxyapatite metal matrix composites. Biomaterials 28, 2163–2174.
Witte, F., Hort, N., Vogt, C., Cohen, S., Kainer, K.U., Willumeit, R., Feyerabend, F., 2008. Degradable biomaterials based on magnesium corrosion. Curr. Opin. Solid State Mater. Sci. 12, 63–72.
Witte, F., Kaese, V., Haferkamp, H., Switzer, E., Meyer-Lindenberg, A., Wirth, C., Windhagen, H., 2005. In vivo corrosion of four magnesium alloys and the associated bone response. Biomaterials 26, 3557–3563.
Wu, C., Chang, J., 2007. Synthesis and in vitro bioactivity of bredigite powders. J. Biomater. Appl. 21, 251–263.
Yi, D., Wu, C., Ma, B., Ji, H., Zheng, X., Chang, J., 2014. Bioactive bredigite coating with improved bonding strength, rapid apatite mineralization and excellent cytocompatibility. J. Biomater. Appl. 28, 1343–1353.
Zheng, Y., Gu, X., Xi, Y., Chai, D., 2010. In vitro degradation and cytotoxicity of Mg/Ca composites produced by powder metallurgy. Acta Biomater. 6, 1783–1791.
Zwierzak, I., Baleani, M., Viceconti, M., 2009. Microindentation on cortical human bone: effects of tissue condition and indentation location on hardness values. Proc. Inst. Mech. Eng. Part H: J. Eng. Med. 223, 913–918.